Controlled Growth of Large-Area, Uniform, Vertically Aligned Arrays of α-Fe₂O₃ Nanobelts and Nanowires

Xiaogang Wen,[†] Suhua Wang,[†] Yong Ding,[‡] Zhong Lin Wang,*,[‡] and Shihe Yang*,[†]

Department of Chemistry, Institute of Nano Science and Technology, The Hong Kong University of Science and Technology, Clear Water Bay, Kowloon, Hong Kong, China, and School of Materials Science and Engineering, Georgia Institute of Technology, Atlanta, Georgia 30332

Vertically aligned iron oxide nanobelt and nanowire arrays have been synthesized on a large-area surface by direct thermal oxidation of iron substrates under the flow of O_2. The effects of reactive gas pressure, composition, and temperature have been systematically studied. It was found that nanobelts (width, tens of nanometers; thickness, a few nanometers) are produced in the low-temperature region (∼700 °C) whereas cylindrical nanowires tens of nanometers thick are formed at relatively higher temperatures (∼800 °C). Both nanobelts and nanowires are mostly bicrystallites with a length of tens of micrometers which grow uniquely along the [110] direction. The growth habits of the nanobelts and nanowires in the two temperature regions indicate the role of growth rate anisotropy and surface energy in dictating the ultimate nanomorphologies.

Introduction

Current challenges in the synthesis of one-dimensional (1D) nanomaterials essentially comprise the controls over a single nanowire and the assembly of an ensemble of nanowires. As far as a single nanowire is concerned, the control of morphology, size, and growth direction is of paramount importance. In particular, different morphologies, such as wire-like, rod-like, belt-like, tube-like, and scroll-like, may have different properties with unique applications. For an ensemble of nanowires, suitable alignment on a substrate is critical to the realization of integrated electronic and photonic nanotechnology. Many methods have been developed for the fabrication of nanowire arrays including template methods,[1−4] catalytic growth,[5−7] Langmuir−Blodgett and fluidic alignment techniques,[8,9] electrospinning,[10] etc. These methods often suffer from the difficulty to form single crystals or the need for tedious posttreatment. Using gas−solid and solution−solid reaction methods, we have recently succeeded in synthesizing nanowire arrays of Cu_2S,[11] $Cu(OH)_2$, and CuO without templates and at low temperatures.[12,13]

α-Fe₂O₃ (hematite) is a semiconductor ($E_g = 2.1$ eV) which is environmentally friendly—nontoxic and corrosion-resistant— and easily obtainable. The use of α-Fe₂O₃ has been demonstrated as a photoanode for photoassisted electrolysis of water,[14] an active component of gas sensors,[15−18] a photocatalyst,[19−21] and an ordinary catalyst.[22,23] Vayssieres et al. used a solution method to synthesize hematite nanorod films,[24,25] and they found that the reduced crystal size yields enhanced photoconversion efficiency and improved photovoltaic response. Although high-quality nanobelts of many metal oxides have been obtained by evaporation of the oxide powders,[26] the synthesis of hematite nanobelts has so far not been achieved using this method. It is worth mentioning that early studies of iron oxidation showed the formation of fiber-like features.[27] Most recently, Fu et al.

synthesized hematite nanowire arrays by reactions of CO_2, SO_2, NO_2, and H_2O with iron substrates.[28] In the present work, we attempted the synthesis of uniform hematite nanobelt and nanowire arrays simply by the reaction of O_2 with flat iron foils under well-controlled conditions and systematically varied some synthetic parameters such as gas pressure and temperature. We report the results in this paper, which encompass mainly the formation of vertically aligned hematite nanobelt arrays at ∼700 °C and cylindrical nanowire arrays at ∼800 °C.

Experiment

The thermal oxidation method was used to synthesize the α-Fe₂O₃ nanobelt and nanowire arrays. The experimental setup consists of a horizontal tube furnace of length 120 cm and diameter 10 cm, a quartz tube 100 cm in length and 5 cm in diameter, and a gas flow/control system. Fresh iron foils (10 mm × 5 mm × 0.25 mm) with a purity of 99.9% (Aldrich) were used as both a reagent and a substrate for the growth of α-Fe₂O₃ nanowires. The iron foils were carefully cleaned with absolute ethanol in an ultrasound bath before being loaded into a quartz boat, which was positioned at the end of the quartz tube. The quartz tube was then mounted in the middle of the tube furnace. A flow of high-purity nitrogen (>99.995%) was first introduced into the quartz tube at a fast rate (∼200 sccm) for 20 min to remove air in the system, and then adjusted to 20 sccm accompanied by a flow of oxygen at a rate of 2−5 sccm. At this time, the tube furnace was heated at a rate of 20 °C/min to the designated temperature. After being held at this temperature for ∼10 h, the O_2 flow was stopped, with only the N_2 gas being kept flowing, and the system was allowed to cool naturally to room temperature. The product samples were then collected, which consisted of a scarlet layer homogeneously coated on the substrate.

The as-prepared products on the substrate were directly subjected to characterizations by scanning electron microscopy (SEM) and powder X-ray diffraction (XRD). For transmission electron microscopic (TEM) observations, the nanowire products were transferred onto carbon-coated copper grids by carefully

* To whom correspondence should be addressed. E-mail: chsyang@ust.hk (S.Y.).
† The Hong Kong University of Science and Technology.
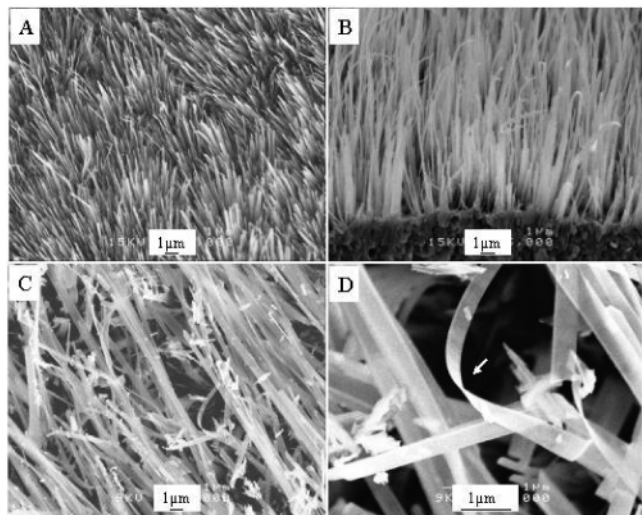‡ Georgia Institute of Technology.

Figure 1. Typical SEM images of the α-Fe$_2$O$_3$ nanobelt array: (A) top view; (B) side view; (C, D) low- and high-magnification images of the nanobelts lying down on the substrate. The nanobelt growth conditions are 700 °C, 5 sccm of O$_2$, and 20 sccm of N$_2$. The reactor pressure was kept at ~1 atm.

Figure 2. SEM images of the α-Fe$_2$O$_3$ nanostructures synthesized at different temperatures: (A) 400 °C; (B) 600 °C; (C) 700 °C; (D) 800 °C. Gas flows: 5 sccm of O$_2$ and 20 sccm of N$_2$.

drawing the surfaces together and gently sliding them over each other. The XRD analyses were performed on a Philips PW-1830 X-ray diffractometer with Cu Kα irradiation ($\lambda = 1.5406$ Å) at a scanning speed of 0.025 deg/s over the 2θ range of 25−75°. The morphologies and elemental compositions of the nanowires were characterized using SEM (JEOL 6300 and JEOL 6300F) at an accelerating voltage of 15 kV. TEM observations were carried out on Philips CM20 and JEOL 2010F and 4000EX microscopes operating at 200 and 400 kV, respectively.

Results

Figure 1 shows SEM images for the samples prepared at 700 °C (20 sccm of N$_2$ and 5 sccm of O$_2$). Clearly, only wire-like features were produced, which are aligned in a dense array approximately perpendicular to the substrate surface (Figure 1A,B). The coverage of the array on the substrate appears to be quite uniform judging from the SEM images. Close examination of SEM images for samples that have been rubbed with a forceps revealed that the wire-like features are actually nanobelts (see Figure 1C,D). The nanobelt morphology is more evident in Figure 1D in which a belt twist with a thickness of several nanometers is portrayed. In fact, belt bending is observed on the top tips of all of the as-grown arrays as can be seen in Figure 1A,B. In general, the nanobelts obtained under our growth conditions are about 5−10 nm in thickness, 30−300 nm in width, and 5−50 μm in length. The width and thickness of a given nanobelt are uniform along the whole length except at the top tip, where thinning and thus bending usually occur.

The temperature dependence of the nanowire growth is presented in Figure 2 in the form of a series of SEM images. At 400 °C, only very few wire-like structures can be observed (Figure 2A), which are meandering and sporadic (Figure 2A). Instead, the surface is mainly covered with seemingly well-crystallized flake-like structures. XRD data have confirmed that the flake-like structures are pure α-Fe$_2$O$_3$. Increasing temperature to 600 °C is accompanied by an increase of the density of the wire-like features and the extent of the alignment (Figure 2B). However, the flake-like structures are still all-pervading. It is worth noting that, without exception, the wire-like features are all grown out of the cleft between the protruding flakes. When temperature is increased to 700 °C, the surface
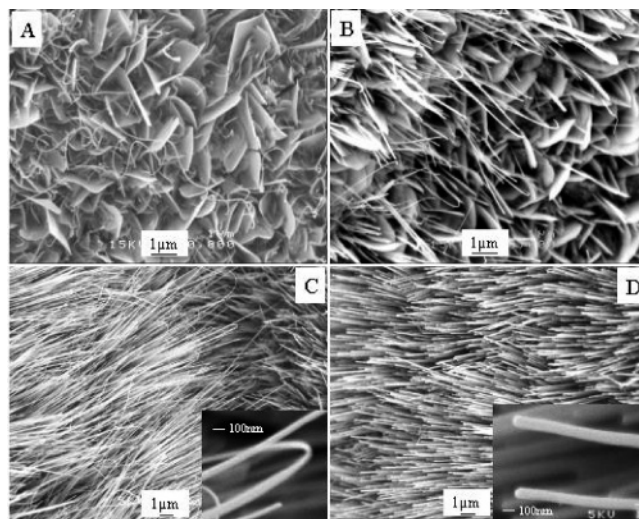
of the substrate is all covered by a dense nanobelt array and no flake-like structure can be found (Figure 2C). Finally, with a further increase of the temperature to 800 °C, the nanobelt array has evolved into an even more uniform array consisting of cylindrical nanowires (Figure 2D). The nanobelt and nanowire morphologies can be appreciated from the insets of Figure 2C,D, respectively. Another distinction lies in the winding top tips of the nanobelts (Figure 2C) and the straightness of the nanowires (Figure 2D). The cylindrical nanowires average ~30−60 nm thick and several tens of micrometers long.

Shown in Figure 3 are XRD patterns of the as-prepared nanobelt (A) and nanowire (B) arrays. It can be seen that both XRD patterns are in conformity with rhombohedral α-Fe$_2$O$_3$ ($a = 5.038$ Å, $c = 13.772$ Å). In the XRD pattern of the nanobelt array, the relative peak intensities of the diffraction planes (110) and (300) are much higher when compared with those of the standard powder diffraction pattern of bulk α-Fe$_2$O$_3$ (Figure 3C). Preferential orientation and alignment of the nanobelt crystals on the substrate are plainly the explanation. As will be described below, the α-Fe$_2$O$_3$ nanobelts grow along the ⟨110⟩ direction, which gives rise to a relatively intense diffraction peak of the (110) plane. We further recall that the nanobelt top tips are generally bowed; the bending is not severe but probably to the extent that the (300) plane becomes roughly parallel to the substrate surface (⟨100⟩ is at an angle of 30° to ⟨110⟩). This explains why the (300) diffraction peak is even much stronger than the (110) diffraction peak. As for the nanowires, although the intensity of the (300) diffraction peak becomes comparable to that of (110), the tilting of the nanowires away from the surface normal is still indicated, which can also be seen from the SEM image in Figure 2D.

TEM data and analyses of the α-Fe$_2$O$_3$ nanobelts grown at 700 °C are given in Figures 4 and 5. After being transferred to the TEM grid, the nanobelts are in a lying-down configuration and still aligned with a regular width of 150−250 nm (Figure 4A). Notice that the nanobelts have been broken at both ends during the sample transfer; what is interesting is that the nanobelt ends are always cleaved at the same angle (~60°) and the cleaved plane is probably (100). Most of these nanobelts have a uniform width (30−300 nm) on the whole length (several to several tens of micrometers), and the thickness of the nanobelts is only about several nanometers (estimated from SEM observations). The high-resolution TEM image of a single nanobelt
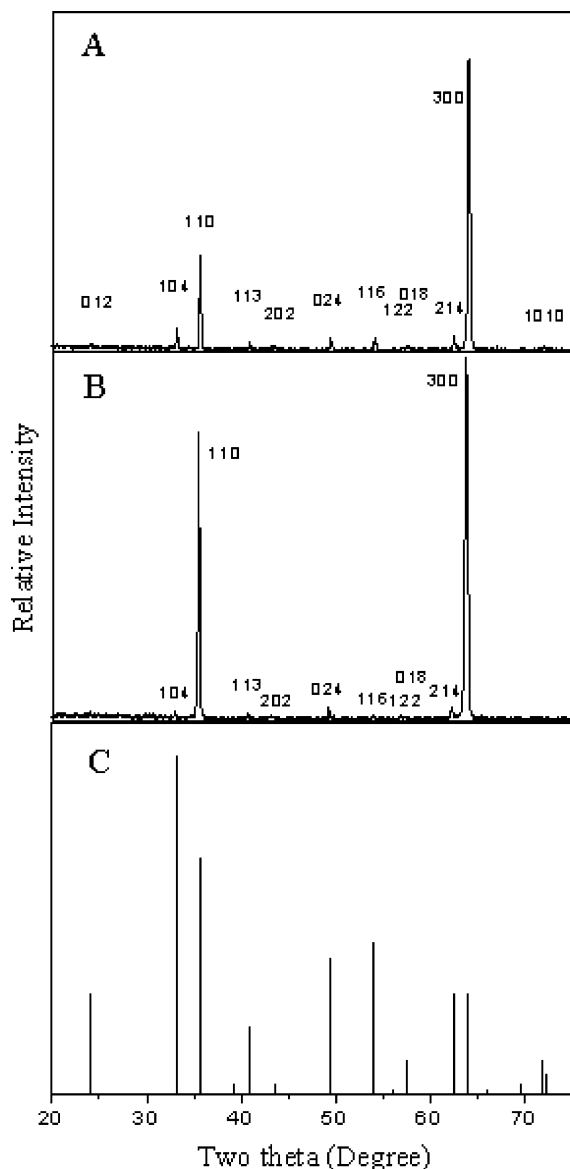
Growth of α-Fe$_2$O$_3$ Nanobelts and Nanowires

J. Phys. Chem. B, Vol. 109, No. 1, 2005 **217**

Figure 3. XRD patterns of the vertically aligned α-Fe$_2$O$_3$ nanobelt array (A, as prepared at 700 °C) and nanowire array (B, as prepared at 800 °C). (C) Standard XRD pattern of α-Fe$_2$O$_3$ powder.
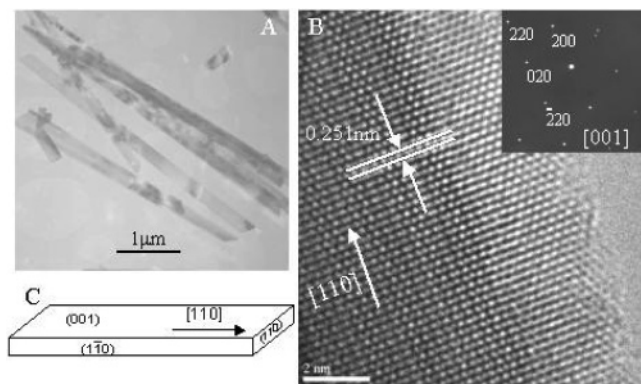

Figure 4. Structure of the α-Fe$_2$O$_3$ nanobelts prepared at 700 °C: (A) low-magnification TEM image of the nanobelts; (B) HRTEM image of a single nanobelt along with an ED pattern (inset); (C) a structural model of the α-Fe$_2$O$_3$ nanobelts.

(Figure 4B) exhibits clear fringes perpendicular to the nanobelt axis. The fringe spacing measures 0.251 nm, which concurs well with the interplanar spacing of (110) and alludes to the nanobelt growth direction along [110]. This is consistent with the selected
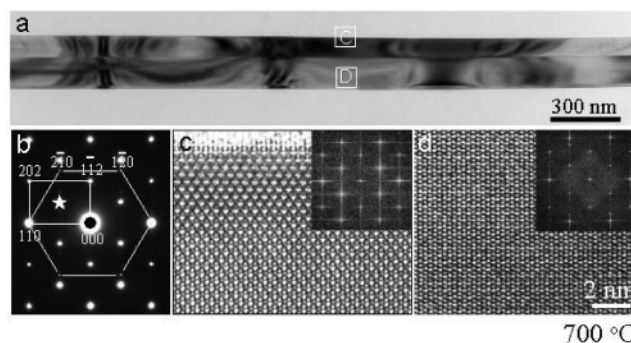

Figure 5. (a) Bright-field TEM image of the Fe$_2$O$_3$ nanobelt in the 700 °C temperature zone. (b) SAED pattern of the nanobelt in (a). (c, d) HRTEM images recorded from the rectangles C and D enclosed areas in (a). Their FFTs are shown in the insets.

area electron diffraction (SAED) pattern in the inset of Figure 4B, which is indexed to the [001] zone axis of rhombohedral α-Fe$_2$O$_3$. On the basis of the XRD, TEM, and SAED results presented above, a structural model of the α-Fe$_2$O$_3$ nanobelts is put forward in Figure 4C, which extends along [110] and is enclosed by the top/bottom surfaces (001)/(00$\bar{1}$) and the side surfaces (1$\bar{1}$0)/($\bar{1}$10).

If examined carefully, extra weak diffraction spots exist in the inserted SAED pattern in Figure 4. Figure 5 is used to characterize the local structural details of these nanobelts. Figure 5a is a bright-field image of a single nanobelt obtained at 700 °C. The SAED pattern in Figure 5b is composed of two sets of diffraction patterns, which correspond to an electron beam parallel to the [001] and [$\bar{1}$11] directions. The image contrast suggests a boundary in the middle of the belts. The high-resolution TEM (HRTEM) images from the rectangles C and D enclosed areas are displayed in Figure 5c,d. The inset in each of them is the fast Fourier transform (FFT) of the corresponding HRTEM image, which indicates that the D area, bottom part of the belt, is composed of at least two overlapped grains to form a bicrystal structure. The two overlapped grains share the same [110] direction. One of the grains is comparably large and crosses the whole width of the belt as the FFTs indicate.

Figure 6 displays TEM images of the α-Fe$_2$O$_3$ nanowires synthesized at 800 °C. After being transferred to the copper grids, the nanowires look more twisted. In general, the nanowires are much thinner ($d = \sim$40 nm) than the nanobelts shown in Figure 4. The TEM images indicate that the products synthesized at high temperature are not belt-like but probably cable-like judging from the uniform thickness along the wires in the bending configurations. This is consistent with the inference above. The stronger set diffraction spots in the inset of Figure 6A are assigned with the [1$\bar{1}$1] zone axis of α-Fe$_2$O$_3$. Furthermore, the HRTEM image of a single nanowire shows regular fringes ($d = 0.251$ nm) perpendicular to the axial direction, suggesting the same growth direction as for the nanobelts, i.e., [110]. Surprisingly, we also found that at least some nanowires possess a scroll-like structure as can be seen in the bottom left inset of Figure 6C. Here roughly four rolling layers can be recognized at the tip, which form a cylindrical nanoscroll with a diameter of 40 nm. The top right inset of Figure 6 shows a bright-field HRTEM image of the same nanowire in the middle portion. Clearly, the edge area is lighter compared to the inner region and exhibits a better contrast because it is only a single sheet extending out. Regular fringes are also observed perpendicular to the wire axis with a spacing of 0.251 nm. This indicates that the rolling direction of the sheet is perpendicular to [110].
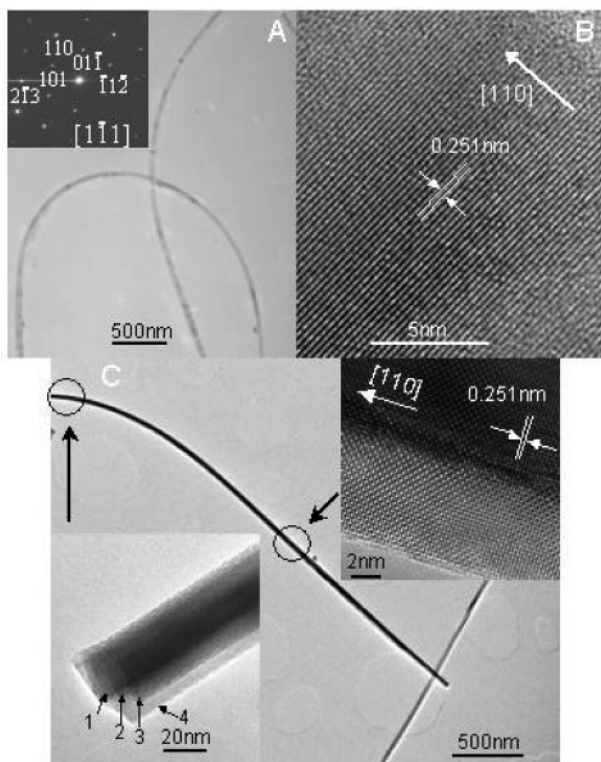
Figure 6. Structure of the α-Fe$_2$O$_3$ nanowires and nanoscrolls prepared at 800 °C: (A) low-magnification TEM image of the nanowires along with an ED pattern of a single nanwire (inset); (B) HRTEM image of a single nanowire; (C) low-magnification TEM image of a single nanosroll. Bottom left inset: high-magnification TEM image of the nanoscroll tip. Top right inset: HRTEM image of the same nanoscroll in the shaft region.
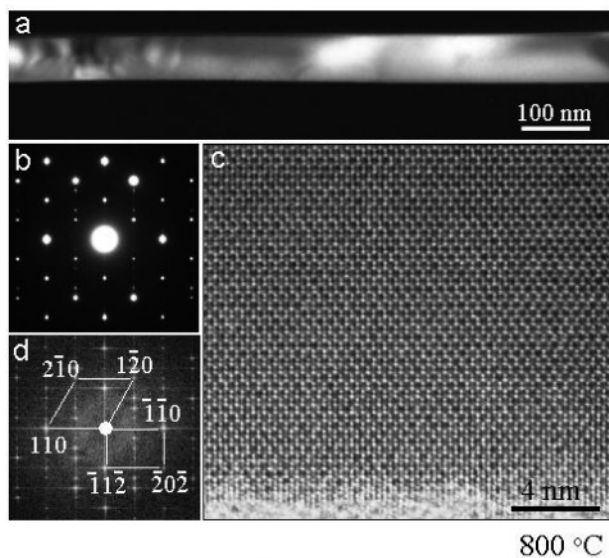

Figure 7. (a) Dark-field TEM image of the Fe$_2$O$_3$ nanowire in the 800 °C temperature zone. (b) SAED pattern of the nanowire in (a). (c) HRTEM image recorded from the nanowire in (a). The FFT of the HRTEM image is shown in (d), which is consistent with the SAED pattern (b).

Shown in Figure 7 is a nanowire prepared at 800 °C. The diffraction contrast in Figure 7a suggests its wire morphology. The SAED pattern in Figure 7b is the same as that in Figure 5b, indicating the bicrystal structure. The FFT (Figure 7d) from the HRTEM image (Figure 7c) recorded from the wire conforms to its bicrystal structure. It is clear that most of the synthesized α-Fe$_2$O$_3$ nanobelts and nanowires have a bicrystal structure and
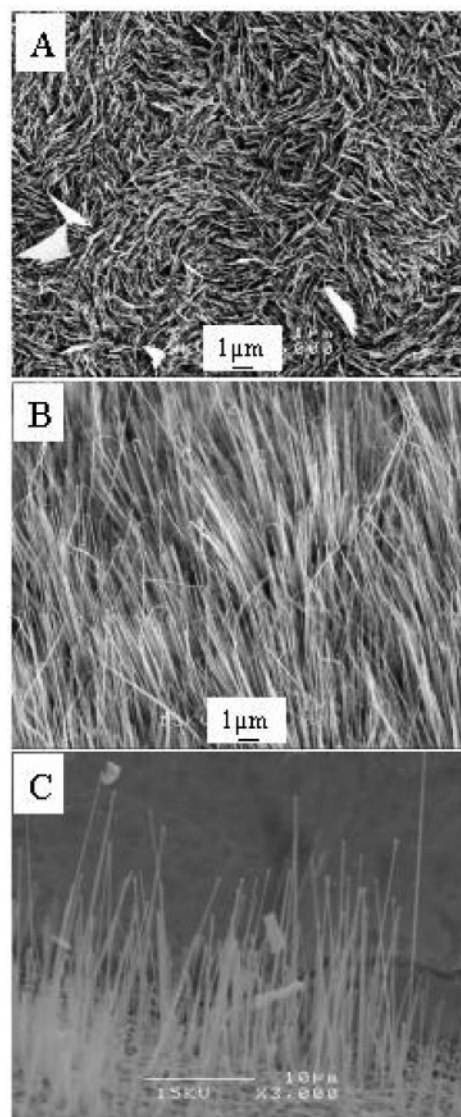

Figure 8. SEM images of the α-Fe$_2$O$_3$ nanostructures synthesized under different gas flow conditions: (A) in air; (B) N$_2$ (20 sccm) + O$_2$ (5 sccm); (C) pure O$_2$ (25 sccm).

the nanostructures grow uniquely along the [110] direction. The bicrystal structure cannot be indexed as a twin because the normal twin planes in bulk α-Fe$_2$O$_3$ are the basal plane (001) and the *R*-plane {012}.[29,30]

We also studied the α-Fe$_2$O$_3$ nanowire growth under the same flow conditions but with different gas compositions. The results for the 700 °C growth are shown in Figure 8. When the preparation was carried out in the static laboratory air, interconnected rod-like structures 30−60 nm in diameter were formed with random orientations (Figure 8A). In addition, some flake-like structures can also be found. The random orientations of the nanorods may be caused by the static gas condition. We next tested mixtures of flowing O$_2$ and N$_2$. With O$_2$ (5 sccm) and N$_2$ (20 sccm), the surface of the substrate was covered with a well-aligned Fe$_2$O$_3$ nanobelt array (Figure 8B). However, in the atmosphere of pure O$_2$ (25 sccm), only a small amount of wire-like features were obtained (Figure 8C), which were not uniform and poorly oriented. The nanowires synthesized under this condition seem to be cylindrical, which are found to be more brittle in a way similar to that from the high-temperature synthesis. Taken together, there is a large influence of the rate of oxidation on the nucleation and growth of the 1D nanostructures.
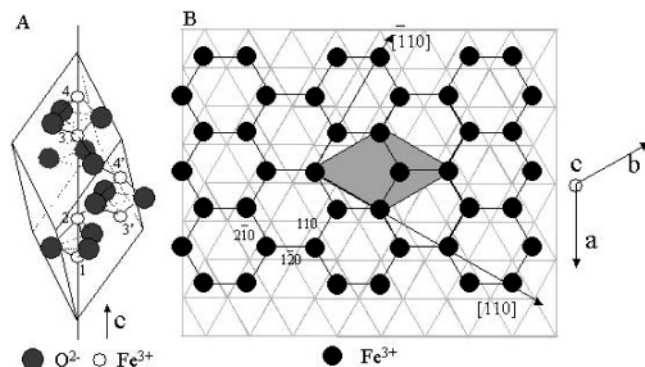
Growth of α-Fe₂O₃ Nanobelts and Nanowires

J. Phys. Chem. B, Vol. 109, No. 1, 2005 **219**

Figure 9. Unit cell (A) and an O layer/Fe layer alternate packing structure model of α-Fe₂O₃ (B).

Discussion

Our present studies provide some clues to the 1D growth mechanisms of α-Fe₂O₃. Some general remarks are in order. First, due to the very low Fe and α-Fe₂O₃ vapor pressures (the melting points of Fe and α-Fe₂O₃ are 1535 and 1350 °C, respectively)[28] at the temperatures of our syntheses, the 1D growth of α-Fe₂O₃ is inexplicable by the vapor−liquid−solid (VLS) and vapor−solid (VS) mechanisms. The former is rejected by the fact that no spherical particles have been found at the tips of the nanowires, and the latter is ruled out because all of the 1D features we observed were grown out of the substrates and nowhere else did we find any trace of α-Fe₂O₃ nanowires. Second, we have shown that low-temperature synthesis prefers the formation of the nanobelts and high-temperature synthesis favors the growth of the nanowires. This nanobelt-to-nanowire morphology transition is probably related to surface energy and different growth rates along different crystal directions. Third, we have noticed that the nanobelts are all grown out of the gaps between flakes; no nanobelts were nucleated on the well-crystallized flakes. This indicates that the nanobelts grow from defects such as planar defects of twins and grain boundaries. Finally, our results tend to support the tip-growth mechanism, which was proposed by Takagi et al.[27] With the lapse of reaction time, narrowing and thinning of the nanobelts occur. If a root-growth mechanism were operative, the nanobelt root would appear to grow wider and wider with time. This is not expected because the diffusion of O₂ to the root region should be more restricted as the nanobelts grow longer.

A structure model of hematite is sketched in Figure 9 to illustrate the growth of the nanobelts and nanowires. As can be seen from Figure 9A, the structure comprises the alternate layers of O triangle nets (A and B) and Fe hexagonal nets (c₁, c₂, and c₃) in the sequence of Ac₁Bc₂Ac₃Bc₁Ac₂Bc₃....[31] This layer structure can easily account for the smallest dimension of the nanobelts—the thickness—because the layers are close-packed and the layer-by-layer growth is expected to be slow. It can also be seen in Figure 9B that the O atoms are close-packed in the (110) plane, whereas the packing of the Fe atoms in this plane is less close than that in, say, the ($\bar{1}$10) plane. The O-rich and Fe-deficient character of the (110) plane may be the driving force for the preferential growth along the [110] direction. On the basis of the considerations above, surface diffusion of Fe atoms is a determining factor, which brings Fe atoms from the Fe foil base to the nanowire tip to sustain the nanowire growth. Because Fe atoms are more reactive and more deficient in the (110) plane and the Fe diffusion in the [110] direction is more facile, the nanobelt growth along the [110] direction is more favorable as observed.

We are now in a position to rationalize the experimental observations of the hematite nanowire growth. At low temperatures (<400 °C), although surface oxidation does occur, very few hematite nanowires are formed because the Fe surface diffusion is too slow. The surface oxidation mainly produces hematite flakes due to its layer structure. At 600 °C, some fiber-like structures start to grow from the clefts of the flakes due to the increased diffusion rate of Fe in the defect sites. When the temperature is increased to 700 °C, the increased diffusion rate of Fe significantly facilitates the hematite nanobelt growth so that the aligned nanobelts uniformly cover the whole substrate surface. The thinning of the nanobelt tips has resulted in the bending of the tips, which can be explained by the reduced supply of Fe owing to the increased diffusion length. Finally, when the temperature is set at 800 °C, the nanowires are much more straight and their cross section becomes cylindrical, at least some of which having a scroll-type structure. Here the temperature is sufficiently high that the Fe diffusion can maintain the nanowire growth without thinning. Moreover, this temperature is also high enough to induce structure reorganization from a belt to a cylindrical structure so as to minimize the surface energy.

Conclusion

Summarizing, we have successfully synthesized well-aligned hematite nanobelt and nanowire arrays on iron substrates by a simple gas−solid reaction process. The morphologies of the 1D nanostructures can be reasonably controlled by varying the reaction temperature and gas composition. In other words, the lower temperature supports the nanobelt growth, whereas cylindrical nanowires are grown at the higher temperature. At least some cylindrical nanowires synthesized at the higher temperature have a scroll-type structure. We have shown that the nanobelts and nanowires all grow along the [110] direction through the surface diffusion of Fe atoms or ions to the tips of the nanostructures. Interesting bicrystal structures have been revealed, which exist for most of the as-prepared hematite nanobelts and nanowires. The controlled formation of the hematite nanobelt and nanowire arrays promises applications in the areas of nanoelectronics, sensors, batteries, and photocatalysts. It is anticipated that this method can be used to synthesize ordered nanowire arrays of other oxides and chalcogenides.

References and Notes

(1) Brumlik, C. J.; Martin, C. R. *J. Am. Chem. Soc.* **1991**, *113*, 3174.

(2) Fan, R.; Wu, Y. Y.; Li, D. Y.; Yue, M.; Majumdar, A.; Yang, P. D. *J. Am. Chem. Soc.* **2003**, *125*, 5254.

(3) Limmer, S. J.; Cao, G. Z. *Adv. Mater.* **2003**, *15*, 427.

(4) Melosh, N. A.; Boukai, A.; Diana, F.; Gerardot, B.; Badolato, A.; Petroff, P. M.; Heath, J. R. *Science* **2003**, *300*, 112.

(5) Li, W. Z.; Xie, S. S.; Qian, L. X.; Chang, B. H.; Zou, B. S.; Zhou, W. Y.; Zhao, R. A.; Wang, G. *Science* **1996**, *274*, 1701.

(6) Ren, Z. F.; Huang, Z. P.; Xu, J. W.; Wang, J. H.; Bush, P.; Siegal, M. P.; Provencio, P. N. *Science* **1998**, *282*, 1105.

(7) Wang, X. D.; Summers, C. J.; Wang, Z. L. *Nano Lett.* **2004**, *4*, 423.

(8) Huang, Y.; Duan, X. F.; Wei, Q. Q.; Lieber, C. M. *Science* **2001**, *291*, 630.

(9) Yang, P. D. *Nature* **2003**, *425*, 243.

(10) Li, D.; Wang, Y. L.; Xia, Y. N. *Nano Lett.* **2003**, *3*, 1167.

(11) Wang, S. H.; Yang, S. H. *Adv. Mater. Opt. Electron.* **2000**, *10*, 39.

(12) Zhang, W. X.; Wen. X. G.; Yang, S. H.; Berta, Y.; Wang, Z. L. *Adv. Mater.* **2003**, *15*, 822.

(13) Wen, X. G.; Zhang, W. X.; Yang, S. H. *Langmuir* **2003**, *19*, 5898.

(14) Kennedy, J. H.; Anderman, M. *J. Electrochem. Soc.* **1983**, *130*, 848.

(15) Chauhan, P.; Annapoorni, S.; Trikha, S. K. *Thin Solid Films* **1999**, *346*, 266.

(16) Fukazawa, M.; Matuzaki, H.; Hara, K. *Sens. Actuators, B* **1993**, *13*, 521.

(17) Han, J. S.; Bredow, T.; Davey, D. E.; Yu, A. B.; Mulcahy, D. E. *Sens. Actuators, B* **2001**, *75*, 18.

(18) Comini, E.; Guidi, V.; Frigeri, C.; Ricco, I.; Sberveglieri, G. *Sens. Actuators, B* **2001**, *77*, 16.

(19) Ohmori, T.; Takahashi, H.; Mametsuka, H.; Suzuki, E. *Phys. Chem. Chem. Phys.* **2000**, *2*, 3519.

(20) Frank, S. N.; Bard, A. J. *J. Phys. Chem.* **1977**, *81*, 1484.

(21) Faust, B. C.; Hoffmann, M. R.; Bahnemann, D. W. *J. Phys. Chem.* **1989**, *93*, 6371.

(22) Weiss, W.; Zscherpel, D.; Schlogl, R. *Catal. Lett.* **1998**, *52*, 215.

(23) Gues, J. W. *Appl. Catal.* **1986**, *25*, 313.

(24) Vayssieres L.; Hagfeldt, A.; Lindquist, S. E. *Pure Appl. Chem.* **2000**, *72*, 47.

(25) Beermann, N.; Vayssieres L.; Lindquist, S. E.; Hagfeldt, A. *J. Electrochem. Soc.* **2000**, *147*, 2456.

(26) Pan, Z. W.; Dai, Z. R.; Wang, Z. L. *Science* **2001**, *291*, 1947.

(27) Takagi, R. *J. Phys. Soc. Jpn.* **1957**, *12*, 1212.

(28) Fu, Y. Y.; Wang, R. M.; Xu, J.; Chen, J.; Yan, Y.; Narlikar, A. V.; Zhang, H. *Chem. Phys. Lett.* **2003**, *379*, 373.

(29) Bursill, L. A.; Peng, J. L. *Philos. Mag. Lett.* **1989**, *60*, 1−10.

(30) Rursill, L. A.; Withers, R. L. *Philos. Mag. A* **1979**, *40*, 213−232.

(31) Watanabe, Y.; Ishii, K. *Phys. Status Solidi A* **1995**, *150*, 673.